JACS
JOURNAL OF THE AMERICAN CHEMICAL SOCIETY
Article
pubs.acs.org/JACS

# Nanostructured Ternary FeCrAl Oxide Photocathodes for Water Photoelectrolysis

Ilina Kondofersky,[†,⊥] Alexander Müller,[†,‡,⊥] Halina K. Dunn,[†] Alesja Ivanova,[†] Goran Štefanić,[§] Martin Ehrensperger,[†] Christina Scheu,[‡] Bruce A. Parkinson,[∥] Dina Fattakhova-Rohlfing,[†] and Thomas Bein*[,†]

[†]Department of Chemistry and Center for NanoScience (CeNS), Ludwig-Maximilians-Universität München, Butenandtstr. 5-13 (E), 81377 Munich, Germany

[‡]Max-Planck-Institut für Eisenforschung GmbH, Max-Planck-Straße 1, 40237 Düsseldorf, Germany

[§]Division of Materials Chemistry, Ruđer Bošković Institute, P.O. Box 180, 10002 Zagreb, Croatia

[∥]Department of Chemistry and School of Energy Resources, University of Wyoming, 1000 East University Avenue, Laramie, Wyoming 82071, United States

Supporting Information

**ABSTRACT:** A sol−gel method for the synthesis of semiconducting FeCrAl oxide photocathodes for solar-driven hydrogen production was developed and applied for the production of meso- and macroporous layers with the overall stoichiometry $Fe_{0.84}Cr_{1.0}Al_{0.16}O_3$. Using transmission electron microscopy and energy-dispersive X-ray spectroscopy, phase separation into Fe- and Cr-rich phases was observed for both morphologies. Compared to prior work and to the mesoporous layer, the macroporous FeCrAl oxide photocathode had a significantly enhanced photoelectrolysis performance, even at a very early onset potential of 1.1 V vs RHE. By optimizing the macroporous electrodes, the device reached current densities of up to 0.68 mA $cm^{-2}$ at 0.5 V vs RHE under AM 1.5 with an incident photon-to-current efficiency (IPCE) of 28% at 400 nm without the use of catalysts. Based on transient measurements, this performance increase could be attributed to an improved collection efficiency. At a potential of 0.75 V vs RHE, an electron transfer efficiency of 48.5% was determined.

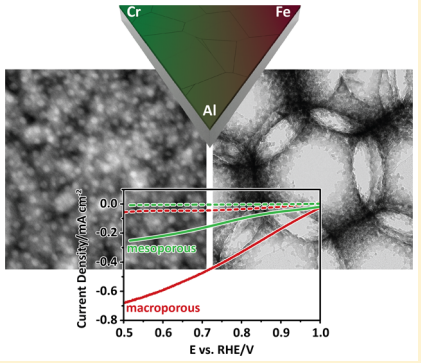


## INTRODUCTION

Solar energy is becoming increasingly important as an abundant and renewable energy source, and the photoelectrolysis of water using illuminated semiconductor electrodes is considered an important technology for the generation of hydrogen in a sustainable and efficient way.[1] The most critical issue for the development of photoelectrolysis cells is the development of suitable photoabsorber materials that combine stability and efficient solar light harvesting with fast kinetics of the interfacial water splitting reactions.[2] To date, numerous material systems have been investigated. Among those more intensively studied as photoanode materials are $BiVO_4$,[3] $\alpha$-$Fe_2O_3$,[4] $WO_3$,[5] and $TiO_2$[6] and, as photocathode materials, p-Si,[7] $Cu_2O$,[8] or $CuFeO_2$.[9] However, in spite of significant efforts, the progress toward efficient solar water splitting systems has been slow. The efficiency of all known photoabsorbers is limited by factors such as poor light harvesting, losses caused by inefficient electron−hole pair separation, bulk and interfacial recombination or high overpotentials for the overall water splitting reaction, and instability of the photoelectrodes. Consequently, discovering and optimizing novel photoabsorber materials is important for the development of competitive photoelectrochemical cells. This is a very demanding task due to the practically unlimited number of potential material classes and combinations of elements. An extremely powerful approach is offered by high-throughput theoretical[10,11] and experimental[12−18] screening methods. However, the identification of promising materials with specific stochiometrics is only the first step and, aided by characterization and increasing understanding of material properties, synthesis strategies have to be refined to obtain electrodes with optimized compositions and morphologies.

Recently, the Solar Hydrogen Activity research Kit (SHArK) project, a distributed science research project,[19] identified a p-type ternary oxide semiconductor containing the earth-abundant and inexpensive elements Fe, Cr, and Al. Combinatorial optimization identified the highest photoelectrolysis activity for the hydrogen evolution reaction at a stoichiometry near $Fe_{0.84}Cr_{1.0}Al_{0.16}O_3$. The discovered material features a band gap of 1.8 eV. While the incident photon-to-current efficiency (IPCE) of around $1 \times 10^{-4}$ % at 500 nm is very low, a promising photovoltage of around 0.95 V was reached. Sliozberg et al.[20] obtained higher photocurrents of 10 $\mu$A $cm^{-2}$ at 0.5 V vs RHE under AM 1.5 with an IPCE of 0.3%

**Received:** July 31, 2015
**Published:** January 8, 2016





DOI: 10.1021/jacs.5b08040
J. Am. Chem. Soc. 2016, 138, 1860−1867

at 350 nm by depositing thicker films using reactive magnetron co-sputtering, demonstrating that the performance of this material can be improved by employing different fabrication routes.

Inspired by the potential of this recently discovered material, we focused on the development of large-scale photocathode morphologies based on ternary FeCrAl oxides. We report a sol–gel synthesis method that yielded mesoporous thin films with photocurrents of 0.25 mA $cm^{-2}$ at 1.23 V vs RHE and an early photocurrent onset at 1.1 V vs RHE. The performance can be improved further by introducing a template and synthesizing a periodic, porous inverse-opal structure. After optimization, a photocurrent of 0.68 mA $cm^{-2}$ under AM 1.5 illumination with an IPCE of 28% at 400 nm was reached while retaining the early onset potential. We further describe extensive structural and electrochemical studies aimed at understanding the correlation between synthesis conditions, structure, and photoelectrochemical behavior of the novel material.

## EXPERIMENTAL SECTION

Mesoporous FeCrAl oxide layers were prepared by dissolving the precursor salts $Fe(NO_3)_3{\cdot}9H_2O$, $Cr(NO_3)_3{\cdot}9H_2O$, and $Al(NO_3)_3{\cdot}9H_2O$ in ethanol, resulting in 0.5 M solutions. The precursor solutions were mixed in a ratio of 0.42:0.5:0.08, respectively, to achieve the targeted composition. This solution was spin coated (800 rpm for 30 s) onto fluorine-doped tin oxide glass, FTO (TEC 15 Glass, Dyesol), resulting in films that were calcined at 525 °C for 1.5 h (2 °C/min heat ramp).

Macroporous films were synthesized by predepositing poly(methyl methacrylate) (PMMA) spheres as a template. PMMA spheres with a diameter of 300 nm were prepared according to a procedure previously described by us.[21,22] In brief, the particles were synthesized by adding methyl methacrylate (MMA) (35.6 g, 0.35 mol) and sodium dodecyl sulfate (SDS) (5 mg, 0.02 mmol) to deoxygenated water (98 mL) under nitrogen purging at 40 °C. The resulting emulsion was heated to 70 °C for 1 h under reflux and vigorous stirring. The polymerization was initiated by adding potassium peroxydisulfate (56 mg, 0.2 mmol) dissolved in water (2 mL) and stopped after 2.5 h by cooling the suspension to room temperature under atmospheric conditions. The resulting PMMA spheres were washed with water by centrifugation (19 000 rpm, 20 min) and redispersed in water.

The FTO substrates were placed vertically in an aqueous PMMA solution (11 wt %), and the solution was dried overnight at 70 °C. These templated films were infiltrated with the FeCrAl precursor solution via spin coating and calcined at 525 °C for 1.5 h (2 °C/min heat ramp).

X-ray diffraction (XRD) analysis was carried out on a STOE powder diffractometer (Cu $K\alpha_1$, $\lambda$ = 1.5406 Å) equipped with a position-sensitive Mythen-1K detector in transmission geometry. X-ray photoelectron spectroscopy (XPS) measurements of the particles on an FTO substrate were performed using a VSW TA 10 X-ray source, providing Mg $K\alpha$ radiation, and a VSW HA 100 hemispherical analyzer. The samples were cleaned by $Ar^+$ sputtering (VSW AS10 ion source) for 8 min at 1 keV. Scanning electron microscopy (SEM) measurements were performed on a JEOL JSM-6500F with a field emission gun run at 5 kV and equipped with an Oxford energy-dispersive X-ray (EDX) detector. A probe-corrected FEI Titan Themis with an X-FEG source operated at 300 kV was used for transmission electron microscopy (TEM). Bright field (BF) and high-resolution TEM (HRTEM) images as well as diffraction patterns were acquired with a Ceta 16 M camera, scanning, TEM (STEM) images with an annular dark field (ADF) detector, and energy-dispersive X-ray (EDX) spectra and maps with four Super-X Bruker SDD detectors. Samples were prepared either by scraping material off the substrate with a razor blade and depositing it on a holey carbon grid or in a cross-sectional geometry as described by Strecker et al.[23]

Film homogeneity and thickness were measured using a Veeco (Dektak 156) profilometer with a 640 × 489 pixel camera and a diamond tip (radius 12.5 $\mu$m).

UV–vis measurements were performed on a PerkinElmer Lambda 1050 UV/visible/NIR spectrophotometer with an integrating sphere. The absorbance of each sample was calculated from experimental reflectance and transmittance measurements and fully corrected for reflectance and absorbance of the FTO substrate using eq 1 as derived by Klahr et al.[24]

$$\mathrm{Abs_F} = \ln\left(\frac{T_{S+F}/T_S}{1 - \frac{R_{S+F} - R_S}{T_S^2}}\right) \quad (1)$$

In eq 1, $T_S/T_{S+F}$ and $R_S/R_{S+F}$ correspond to the wavelength-dependent transmissions and reflections of the plain ($T_S$ and $R_S$) and the coated substrate ($T_{S+F}$ and $R_{S+F}$), respectively.

Photoelectrochemical measurements were carried out using a $\mu$-Autolab III potentiostat equipped with a FRA2 impedance analyzer. The samples were masked with a Teflon-coated glass fiber adhesive tape, leaving an exposed area of 0.2 $cm^2$. The sample was placed in a quartz cell filled with an aqueous 0.1 M $HClO_4$ electrolyte and connected in a three-electrode mode to the potentiostat with a Ag/AgCl reference electrode and a Pt mesh counter electrode. The films were illuminated through the substrate side using an AM 1.5 solar simulator (Solar Light Model 16S) at 100 mW $cm^{-2}$. Current density-voltage ($J$–$V$) curves were obtained by scanning from positive to negative potentials in the dark or under illumination at a 20 mV/s sweep rate.

Incident photon-to-current efficiency (IPCE) measurements were performed under low-frequency chopped monochromatic light (1 Hz). A 150 W xenon lamp equipped with a monochromator and order-sorting filters was used as a light source. The sample bias was set to 0.75 V vs RHE under simulated solar irradiation. The light intensity reaching the electrode was measured using a certified Fraunhofer ISE silicon reference cell equipped with a KG5 filter.

To estimate the electron transfer efficiency, transient current measurements were performed by illuminating the electrode with a 455 nm light emitting diode. The light was switched on and off every 500 ms, and the current was measured at potentials ranging from 1.0 to 0.5 V vs RHE.

## RESULTS AND DISCUSSION

FeCrAl oxide photocathodes were synthesized via a sol–gel route (Figure 1). Precursor solutions were prepared by dissolving the nitrate salts of $Fe^{3+}$, $Cr^{3+}$, and $Al^{3+}$ in ethanol at a ratio of 0.43:0.5:0.08. This stoichiometry has been discovered via a combinatorial optimization approach and reported to yield the highest IPCE values.[19] The electrodes obtained by spin-coating a freshly prepared precursor solution

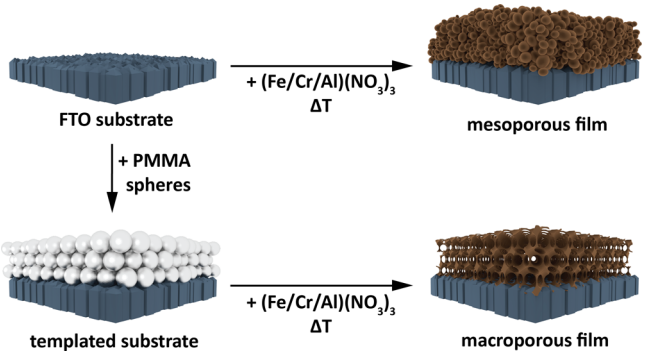


**Figure 1.** Scheme by which mesoporous and macroporous films were synthesized.



DOI: 10.1021/jacs.5b08040
J. Am. Chem. Soc. 2016, 138, 1860–1867

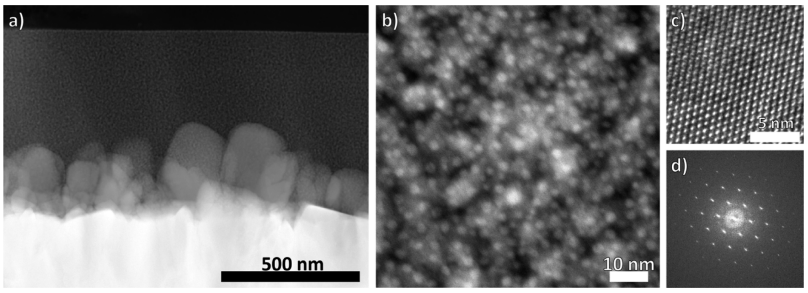


**Figure 2.** TEM images of the mesoporous FeCrAl oxide film. (a) A cross section overview image; (b) an image of the nanoparticles in the Fe-rich region. (c and d) An HRTEM image and the corresponding FFT of the Cr-rich phase. The image shows the (001) plane.

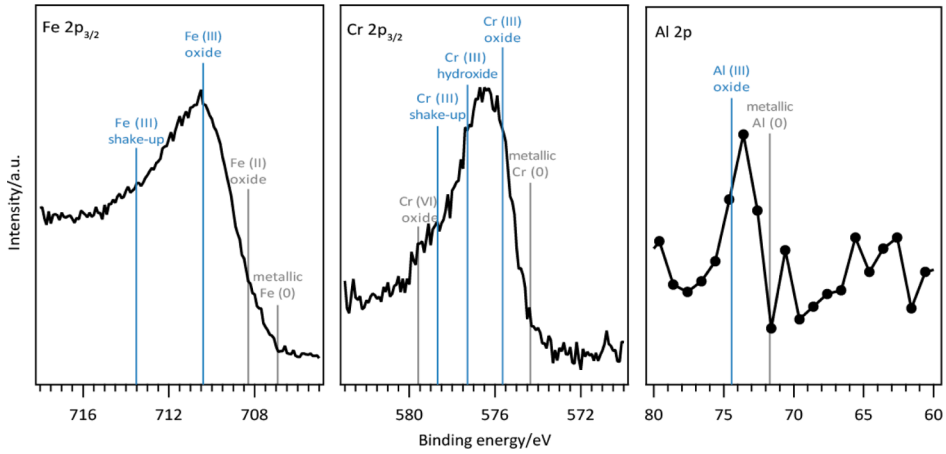


**Figure 3.** X-ray photoelectron spectra of the Fe $2p_{3/2}$, Cr $2p_{3/2}$, and Al 2p edges of the Fe-rich phase in the mesoporous FeCrAl oxide film.

onto FTO and calcining in air at 525 °C are mesoporous and crack-free.

X-ray diffraction patterns of the mesoporous films can be indexed with a single phase having the corundum structure and the space group $R\bar{3}c$. Secondary phases with other crystal structures were not found. The lattice parameters were obtained by a Le Bail[25] refinement (SI Figure 6) as $a$ = 4.9832(1) Å and $c$ = 13.6143(3) Å. This is in excellent agreement (deviation <1%) with the lattice parameters obtained by Rowley et al.[19]

Although XRD analysis of the powder material points to the formation of a single phase, cross section TEM analysis of the films surprisingly reveals a phase separation (Figure 2). The different phases found in TEM could not be resolved by XRD, indicating that both phases form in the corundum structure and have very similar lattice parameters. This was also confirmed by HRTEM measurements and FFT analysis. Near the FTO substrate, a Cr-rich phase with an average Fe:Cr:Al ratio of (20 ± 4: 75 ± 5: 5 ± 1) atom % forms columnar grains with a size of up to 250 nm in the corundum structure. Above this region, a mesoporous network of Fe-rich nanoparticles with an average composition of Fe:Cr:Al = (59 ± 7: 18 ± 4: 23 ± 6) atom % is formed. These can be further separated into large ellipsoid nanoparticles with a diameter of (5.6 ± 0.8) nm decorated with small spherical nanoparticles with a diameter of (1.5 ± 0.2) nm (SI Figure 8). The chemical composition of these particles is slightly different, as the small particles are Al-enriched (Fe:Cr:Al ratio of (71 ± 4: 9 ± 4: 20 ± 6) atom % whereas the large particles have an Fe:Cr:Al ratio of (76 ± 6: 11 ± 2: 13 ± 4) atom %).

X-ray photoelectron spectroscopy was used to detect signals of iron, chromium, and aluminum of the upper, Fe-rich layer of a 500 nm thick, mesoporous FeCrAl oxide film (Figure 3). Peak positions and shapes indicate an oxidation state of +3 for all metal ions. Assignment of the chemical species was done according to Molder et al.[26] Quantification yielded an Fe:Cr:Al ratio of 55:17:28, which is in good agreement with the EDX results. The valence state of Fe was estimated as +3 by comparing the energy positions of the $2p_{3/2}$ peaks to those of the pure oxides[27] (Figure 3). In a similar fashion, the energy position of the Cr $2p_{3/2}$ peak is characteristic for the oxidation state +3.[27,28] The broadening of the peak can be explained either by a shakeup peak or by traces of Cr in a higher oxidation state.[27] As $Cr^{4+}$ and $Cr^{5+}$ compounds are unstable,[29] $Cr^{6+}$ would be most likely, even though the energy shift is not as big as with reference $Cr^{6+}$-containing compounds. Further, no distinct $Cr^{6+}$-containing compounds were found by XRD or TEM, making a shakeup peak and therefore Cr in the oxidation state +3 most likely. Despite the poor energy resolution and the small signal-to-noise ratio, the position of the Al 2p peak supports an $Al^{3+}$-containing oxide.[30] The valence state +3 can therefore be verified for Fe, Cr, and Al in the upper region of the film.

The separation into different phases, all in the corundum structure, is in contrast to previous experimental work, as Steinwehr et al. showed that FeCrAl oxides form solid solutions with a miscibility gap only at high Al-contents.[31] The formation of large, compact Cr-rich nanoparticles at the FTO indicates that a heterogeneous nucleation takes place before other phases form. In accordance, the precursor $Cr(NO_3)_3 \cdot 9H_2O$ is less stable than the other two and dissociates at 100 °C,[32] whereas


DOI: 10.1021/jacs.5b08040
J. Am. Chem. Soc. 2016, 138, 1860−1867

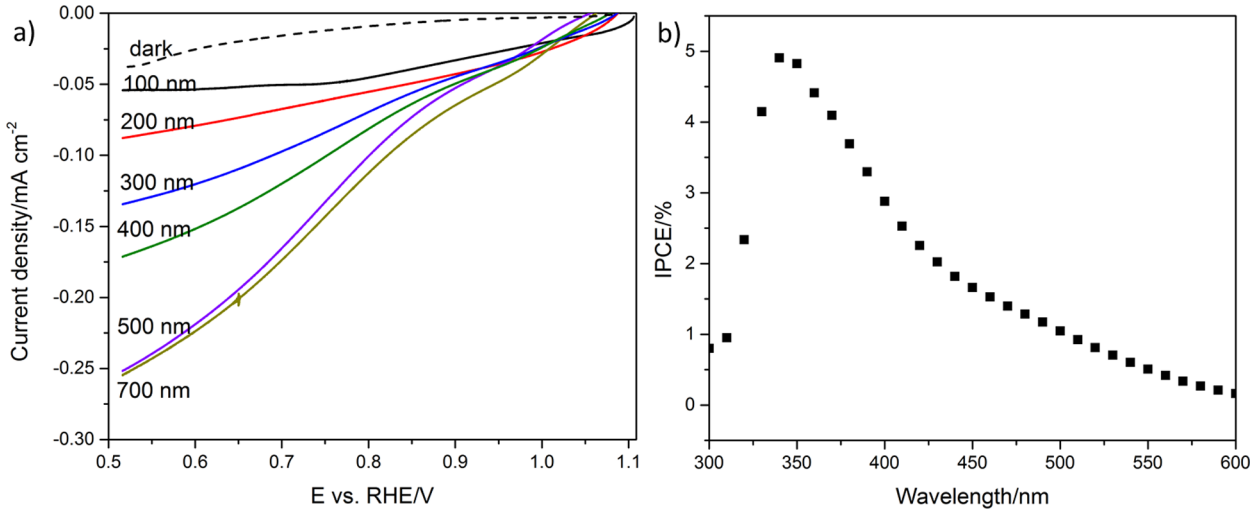


**Figure 4.** (a) Linear sweep voltammograms for mesoporous FeCrAl oxide electrodes in dependence of the film thickness. The samples were illuminated through the substrate with AM 1.5. (b) IPCE spectrum determined for a 500 nm thick mesoporous film on FTO. The drop in photocurrent at 350 nm is attributed to light absorption by the FTO substrate.

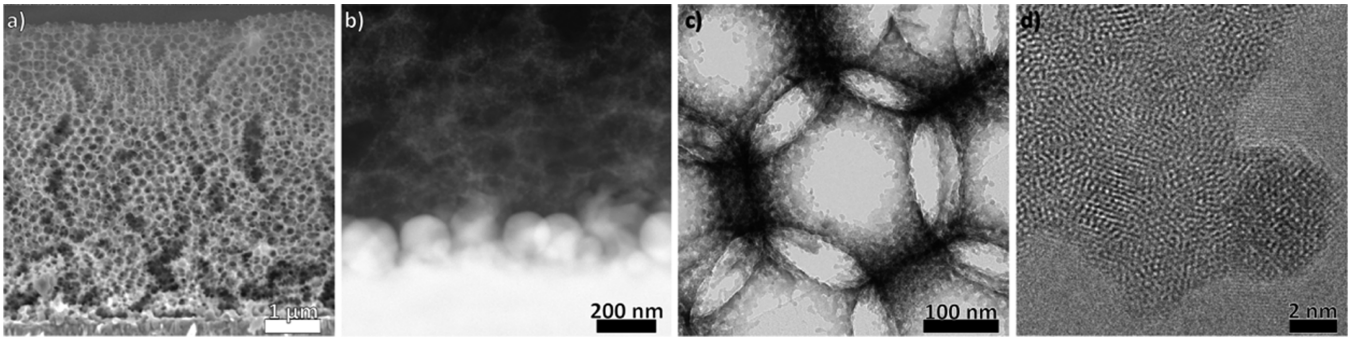


**Figure 5.** (a) Cross-sectional SEM image of a macroporous film. (b) Cross-sectional TEM image of a macroporous film showing the Cr-rich phase near the substrate. (c) BF TEM image of a single pore. (d) HRTEM image of a part of the network.

$Fe(NO_3)_3{\cdot}9H_2O$[33] and $Al(NO_3)_3{\cdot}9H_2O$[34] are stable up to 250 °C. While these temperatures refer to material without solvent, the trend should stay the same, explaining the phase separation. As an alternative synthesis approach, we attempted aging the precursor solution, which led to the spontaneous formation of small nanoparticles with a homogeneous elemental distribution. Experimental details and SEM (SI Figure 3), TEM (SI Figure 1), and elemental composition information (SI Table 1) are provided in the Supporting Information. Films synthesized by depositing these nanoparticles onto FTO, however, led to very low photocurrents (SI Figure 2).

The photoelectrochemical characteristics of mesoporous FeCrAl oxide films of different thicknesses were determined in 0.1 M perchloric acid under AM 1.5 substrate illumination. As expected, the optical absorbance increases linearly with the film thickness (SI Figure 4). The photocurrent densities follow a similar trend, increasing linearly with the thickness up to 0.25 mA $cm^{-2}$ under AM 1.5 (Figure 4a) and an IPCE of 4.9% at 350 nm (Figure 4b) for a 500 nm thick film (SI Figure 10). FeCrAl oxide shows a very early onset potential of 1.1 V vs RHE for a 100 nm thin film. A shift to more negative onset potentials is observed for samples with increasing thickness reaching values of 1.05 V vs RHE for a 500 nm sample. Further, increasing the film thickness leads to a saturation of the photocurrent. This limiting behavior is not observed for thin films of around 40 nm, where the current density remains constant independent of the illumination direction (SI Figure 7). The generated charge carriers can be collected equally well regardless of the sample being illuminated through the substrate or the electrolyte side since most of the light is transmitted, resulting in only a small gradient of carrier concentration across the film and a short path to be collected at the electrode/electrolyte interface. Thicker films have carriers created deeper in the structure and rely on charge carrier transport over long distances across the loosely connected, individual particles.

To enhance the performance, we optimized the electrode morphology by nanostructuring the material. Nanostructuring is a proven strategy for increasing the photogenerated carrier collection efficiency by decoupling the light absorption depth from the charge collection depth.[35−37] Periodic, macroporous morphologies are particularly attractive as they provide both a continuous scaffold for the transport of photogenerated charges to the current collector and a large surface for the heterogeneous charge transfer. Furthermore, the large pore size is beneficial for the infiltration of electrolyte throughout the whole film thickness, for the diffusion of products away from the semiconductor−electrolyte interface, and for lowering the current density and thereby the overpotentials for electrode reactions, respectively. A so-called colloidal crystal templating approach was used to obtain macroporous FeCrAl oxide electrodes using periodic arrays of PMMA beads as a


DOI: 10.1021/jacs.5b08040
J. Am. Chem. Soc. 2016, 138, 1860−1867

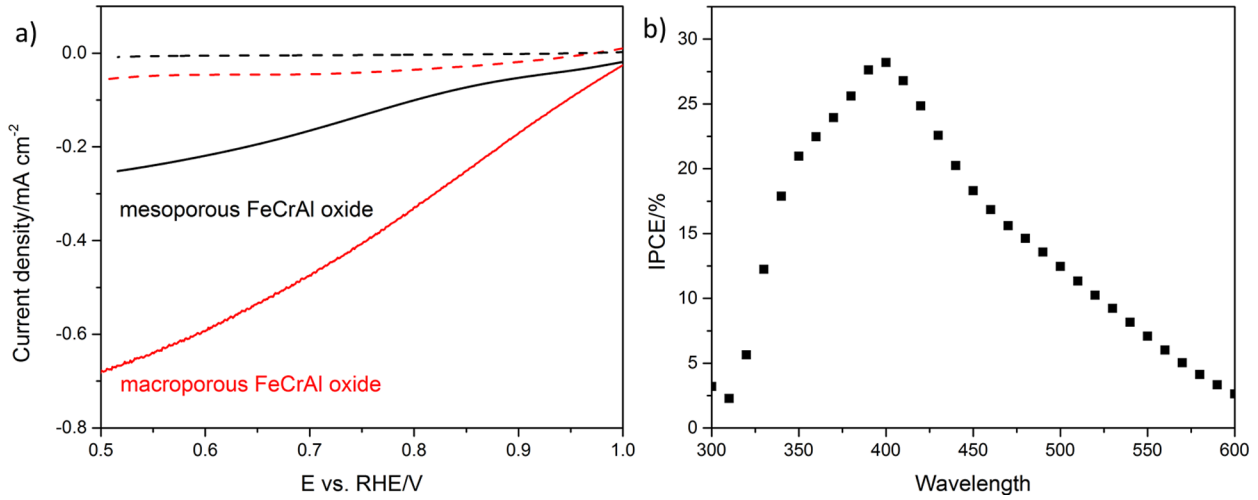


**Figure 6.** (a) Linear sweep voltammograms of the macroporous and mesoporous FeCrAl oxide films with AM 1.5 illumination through the substrate. Dashed curves are dark current sweeps. For comparison, the voltammogram of a 500 nm thick, mesoporous film is also shown. (b) IPCE spectrum determined for the same inverse opal FeCrAl oxide film on FTO.

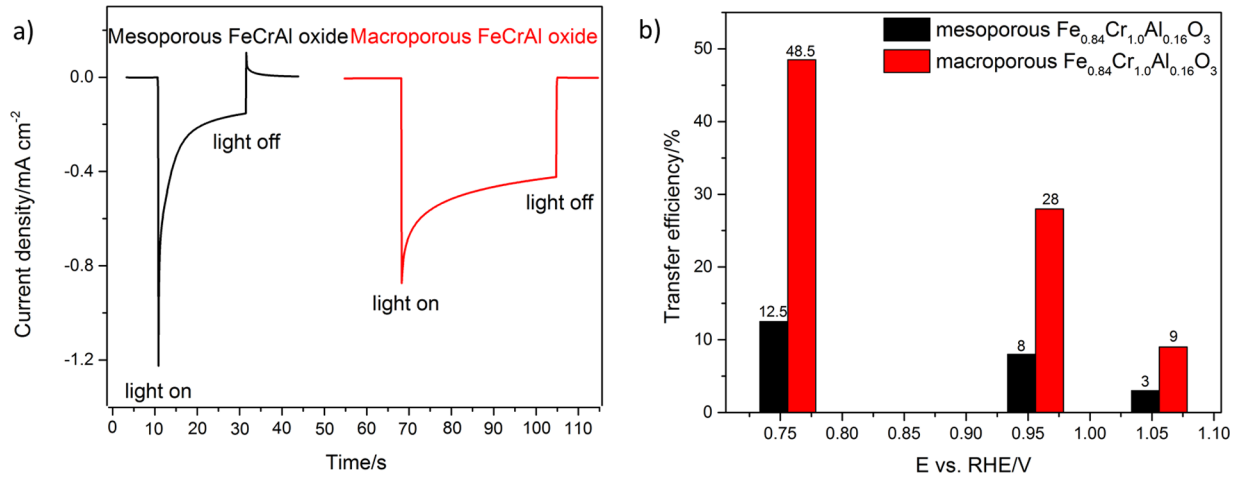


**Figure 7.** (a) Photocurrent transients of a mesoporous and a macroporous FeCrAl oxide film. (b) Transfer efficiency $\eta_{trans}$ determined for mesoporous and inverse opal macroporous FeCrAl oxide films by transient photocurrent response measurements. The samples were illuminated with a 455 nm diode through the substrate side.

template.[38] The PMMA layers were assembled on FTO substrates (SI Figure 5) and impregnated with a freshly prepared sol–gel precursor solution via spin-coating. Calcination leads to decomposition of the precursors and to the combustion of the PMMA template, resulting in crystalline FeCrAl oxide films with a porous, periodic inverse opal structure (Figure 5) with the FeCrAl oxide forming a continuous semiconductor scaffold. The electrodes obtained in this way have a homogeneous thickness ranging from 1 to 6 $\mu$m, good coverage, and a good adhesion to the substrate (Figure 5a). The electrodes used for photoelectrochemical measurements were defined by a film thickness of approximately 3 $\mu$m, having the same light harvesting efficiency as the best performing mesoporous layers of 500 nm and thus allowing a meaningful comparison of films with different morphologies (SI Figure 9).

The average pore diameter of (277 ± 10) nm (Figure 5c) corresponds to a shrinkage by ca. 9% during the calcination process to which we attribute the few defects shown in Figure 5a. As in the case of the mesoporous film, a phase segregation into a Cr-rich phase near the interface with an average composition of Fe:Cr:Al = (9 ± 3: 90 ± 3: 1 ± 1) atom % and a macroporous, Fe-rich phase with an average composition of Fe:Cr:Al = (64 ± 1: 25 ± 4: 11 ± 5) atom % is observed. The Cr-rich phase forms spherical nanoparticles with diameters between 60 and 340 nm. The average composition of the Fe-rich phase was the same over the thickness of the film, and no compositional gradients through the film thickness were detected. HRTEM images show the scaffold to be polycrystalline with small grains on the order of 2 to 4 nm. This leads to improved charge transport properties compared to the mesostructured films, where the individual nanoparticles are only partly connected and charge transport is more difficult.

The photoelectrochemical performance of the macroporous FeCrAl oxide films is shown in Figure 6 and reveals a dramatic photocurrent increase over the mesoporous films. Compared to a 500 nm thick, mesoporous film, the current density is increased by over 60 % reaching a value of 0.68 mA cm$^{-2}$ at 0.5 V vs RHE. Once again of note is the early onset potential of 1.1 V vs RHE. The IPCE of the macroporous film is also increased significantly throughout the whole wavelength range of 300 to 600 nm, reaching a maximum of 28% at 400 nm (Figure 6b).


DOI: 10.1021/jacs.5b08040
J. Am. Chem. Soc. 2016, 138, 1860–1867

The IPCE maximum for macroporous films is red-shifted to 400 nm, compared to the mesoporous film, which has a maximum at 350 nm. This shift is attributed to the inverse opal structure acting as a photonic crystal,[40,41] with transmission measurements (SI Figure 9) confirming a stop band centered at 380 nm. An additional shoulder at 350 nm is at the same position as the maximum measured for mesoporous films and can be attributed to the material itself. The drop at 350 nm is attributed to absorption of light by the FTO substrate.

The transfer efficiency of charges to the electrolyte $\eta_{trans}$ can be assessed from transient current measurements. By illuminating the electrode with chopped light at different chopping frequencies and potentials, photocurrent transients can be measured. From the latter, the instantaneous current density $J_{Inst}$ and the steady-state current density $J_{ss}$ can be determined. For a system where kinetics at the surface are slower than electron generation, $J_{Inst}$ is dominated by perfect electron transfer whereas $J_{ss}$ shows an equilibrium of recombination and transfer. The ratio of $J_{ss}$ and $J_{Inst}$ is therefore a measure of the electron transfer efficiency $\eta_{trans}$[42−45] calculated according to eq 2.

$$\eta_{trans} = \frac{J_{ss}}{J_{inst}} = \frac{k_{trans}}{k_{trans} + k_{rec}} \quad (2)$$

As shown in Figure 7a, the shape of the transients is characteristic for the individual morphologies. The mesoporous sample is characterized by a spiky instantaneous current that decays to a constant steady-state current (Figure 7a). The transient current of the macroporous sample, on the other hand, shows an instantaneous current closer to the steady-state current, indicating a photocurrent response closer to the ideal square shape that is not limited by recombination. This observation is confirmed by determining the transfer efficiencies of both morphologies at different potentials. A 500 nm thick, mesoporous film shows a transfer efficiency of 12.5% at 0.756 V vs RHE. At this potential, at which the current density is 0.13 mA $cm^{-2}$, the transfer efficiency reaches a maximum. Under these conditions, the macroporous film has a transfer efficiency of 48.5%, almost three times as high, indicating superior charge transport properties across the film and explaining the increased transfer efficiency in the macroporous films. The improved electron transfer efficiency has a major contribution to the increased photocurrent shown in Figure 6. The increased transfer efficiency indicates that recombination reactions in either the bulk and/or on the surface are decreased. As the macroporous film has a higher surface area, the surface recombination rate should be higher and the increased transfer efficiency can be attributed to decreased bulk recombination due to the short carrier diffusion length. The short carrier diffusion length requires most photogenerated carriers to be produced in a region where there is a space charge field to separate them. In a more two-dimensional geometry, with the rather low absorption coefficients especially in the red region of the spectrum, most carriers are generated in the bulk of the grains and recombine before they can diffuse to a space charge region. In the macroporous films, the carriers are very likely to be created in or near a region with a space charge field formed by the electrolyte/semiconductor interface. Therefore, there is a higher probability that they will be collected as photocurrent especially in the spectral regions with low absorption coefficients.

The presence of metal oxide phases with different composition raises the question about the photoelectrochemical activity of each individual phase. Theoretical work by Praveen et al.[46] has shown that the band gap can be tuned between 2.5 and 3.1 eV by varying the Fe:Cr:Al ratio. Phase separation can therefore lead to the efficient absorption of large parts of the solar spectrum. In addition, both Cr- and Al-doping of hematite improve charge transport properties.[47−49] Even the formation of the Cr-rich phase can enhance the properties, as $Cr_2O_3$ has been shown to act both as a catalyst and as an oxygen barrier, preventing the direct formation of water from hydrogen and oxygen.[50,51]

Photoelectrochemical characterization of the electrodes revealed that the macroporous structure was beneficial not only for the device architecture, regarding the solid to electrolyte junction, but also for the charge transport across the metal oxide film. Macroporous structures show a nearly 3-fold increase of current density compared to the mesoporous FeCrAl oxide film, reaching values of up to 0.68 mA $cm^{-2}$ at 0.5 V vs RHE under AM 1.5 without any additional catalysts. Compared to devices reported so far in the literature, we demonstrate a 68-fold current density increase[20] as a result of introducing macropores. The main contribution to this electrochemical performance was achieved by the increased electron transfer efficiency to the electrolyte and therefore reduced recombination.

The macroporous FeCrAl oxide photoabsorber shows the highest currents not only for this particular system but, to our knowledge, also among the published metal oxide photocathodes. The best known example for a metal oxide photocathode, $Cu_2O$,[8] reaches current densities of about 0.8 mA $cm^{-2}$ at 0 V vs RHE under uncatalyzed conditions with a photocurrent onset at 0.4 V vs RHE. $CuFeO_2$[9] on the other hand shows a current density of about 20 $\mu$A $cm^{-1}$ at 0 V vs RHE in a non-oxygen-saturated electrolyte with a photocurrent onset at about the same potential. In contrast, the macroporous FeCrAl oxide electrodes have a very early onset potential of 1.1 V vs RHE. At potentials at which we observe 0.68 mA $cm^{-2}$ (0.5 V vs RHE), very little photocurrent is observed for $Cu_2O$ and $CuFeO_2$. This study therefore exemplifies the importance of finding and developing new promising metal oxides as photoelectrodes for water splitting.

## CONCLUSION

We presented the synthesis and characterization of semiconducting FeCrAl oxide photocathodes with different porous morphologies and investigated them for solar-driven hydrogen evolution. Mesoporous FeCrAl oxide films with a photocurrent onset at 1.1 V vs RHE were synthesized using a novel sol−gel synthesis to generate large area crack-free films that were characterized and had their thickness optimized to reach a current density of 0.25 mA $cm^{-2}$ under AM 1.5 at 0.5 V vs RHE with an IPCE of 4.9%. EDX measurements performed with TEM showed that a phase separation occurs, with a Cr oxide rich phase adjacent to the substrate and a Fe rich oxide phase on the top. Template synthesis of an inverse opal macroporous $Fe_{0.84}Cr_{1.0}Al_{0.16}O_3$ electrode drastically increased the photocurrent to 0.68 mA $cm^{-2}$ under AM 1.5 at 0.5 V vs RHE and an IPCE of 28% at 400 nm without the use of hydrogen evolution catalysts. The collection of minority carriers at the semiconductor/electrolyte interface increased nearly 4 times compared to the optimized mesoporous electrode, the highest reported so far for this novel material, showing that it is a


DOI: 10.1021/jacs.5b08040
J. Am. Chem. Soc. 2016, 138, 1860−1867

promising candidate for photoelectrochemical water splitting. Further studies on different morphologies and architectures could additionally improve the device performance. This work shows the potential of nanostructured multinary mixed metal oxides as electrode materials for photoelectrochemical water splitting.

## ■ ASSOCIATED CONTENT

### Supporting Information

The Supporting Information is available free of charge on the ACS Publications website at DOI: 10.1021/jacs.5b08040.

Detailed information regarding XRD, SEM, and electrochemical characterization of the FeCrAl oxide electrodes (PDF)

## ■ AUTHOR INFORMATION


### Corresponding Author

*bein@lmu.de

### Author Contributions

⊥I.K. and A.M. contributed equally.


### Notes

The authors declare no competing financial interest.

## ■ ACKNOWLEDGMENTS

The work was supported by the German Research Foundation (DFG) via the SPP 1613, the Nanosystems Initiative Munich (NIM) and LMUexcellent funded by the DFG, the Bavarian research network 'Solar Technologies Go Hybrid', and the Center for Nanoscience (CeNS). We thank the students Nedzada Imamovic, Chih-Chun Huang, Zachary Edelen, Sabine Sappler and Marina Polo Collado for participating in the research. The authors gratefully acknowledge electron microscopy measurements by Steffen Schmidt and insightful discussions with Alexander Hufnagel. Bruce A. Parkinson acknowledges funding from the Division of Chemical Sciences, Geosciences, and Biosciences, Office of Basic Energy Sciences of the U.S. Department of Energy through Grant No. DE-FG02-05ER15750. The SHArK project was initially funded by a Dreyfus Grant and has recently been supported by the NSF Funded Center for Chemical Innovation entitled "Powering the Planet" under Grant No. CHE-1305124. Bruce A. Parkinson also acknowledges support from the Humboldt Foundation.

## ■ REFERENCES


(1) Grätzel, M. *Nature* **2001**, *414*, 338−344.
(2) Walter, M. G.; Warren, E. L.; McKone, J. R.; Boettcher, S. W.; Mi, Q.; Santori, E. A.; Lewis, N. S. *Chem. Rev.* **2010**, *110*, 6446−6473.
(3) Abdi, F. F.; Han, L.; Smets, A. H. M.; Zeman, M.; Dam, B.; van de Krol, R. *Nat. Commun.* **2013**, *4*, 2195−2197.
(4) Sivula, K.; Le Formal, F.; Grätzel, M. *ChemSusChem* **2011**, *4*, 432−449.
(5) Tacca, A.; Meda, L.; Marra, G.; Savoini, A.; Caramori, S.; Cristino, V.; Bignozzi, C. A.; Pedro, V. G.; Boix, P. P.; Gimenez, S.; Bisquert, J. *ChemPhysChem* **2012**, *13*, 3025−3034.
(6) Fujishima, A.; Honda, K. *Nature* **1972**, *238*, 37−38.
(7) Dominey, R. N.; Lewis, N. S.; Bruce, J. A.; Bookbinder, D. C.; Wrighton, M. S. *J. Am. Chem. Soc.* **1982**, *104*, 467−482.
(8) Paracchino, A.; Laporte, V.; Sivula, K.; Grätzel, M.; Thimsen, E. *Nat. Mater.* **2011**, *10* (6), 456−461.
(9) Prévot, M. S.; Guijarro, N.; Sivula, K. *ChemSusChem* **2015**, *8*, 1359−1367.
(10) Castelli, I. E.; Olsen, T.; Datta, S.; Landis, D. D.; Dahl, S.; Thygesen, K. S.; Jacobsen, K. W. *Energy Environ. Sci.* **2012**, *5*, 5814−5819.
(11) Castelli, I. E.; Landis, D. D.; Thygesen, K. S.; Dahl, S.; Chorkendorff, I.; Jaramillo, T. F.; Jacobsen, K. W. *Energy Environ. Sci.* **2012**, *5*, 9034−9043.
(12) Woodhouse, M.; Parkinson, B. A. *Chem. Soc. Rev.* **2009**, *38*, 197−210.
(13) Woodhouse, M.; Parkinson, B. A. *Chem. Mater.* **2008**, *20*, 2495−2502.
(14) Parkinson, B. *Energy Environ. Sci.* **2010**, *3*, 509−511.
(15) Anunson, P. N.; Winkler, G. R.; Winkler, J. R.; Parkinson, B. A.; Schuttlefield Christus, J. D. *J. Chem. Educ.* **2013**, *90*, 1333−1340.
(16) Borgmann, S.; Schuhmann, W.; Potyrailo, R.; Mirsky, V. *Combinatorial Methods for Chemical and Biological Sensors*; Springer: New York, 2009; pp 331−370.
(17) Sliozberg, K.; Schäfer, D.; Meyer, R.; Ludwig, A.; Schuhmann, W. *ChemPlusChem* **2015**, *80*, 136−140.
(18) Schuppert, A. K.; Savan, A.; Ludwig, A.; Mayrhofer, K. J. J. *Electrochim. Acta* **2014**, *144*, 332−340.
(19) Rowley, J. G.; Do, T. D.; Cleary, D. A.; Parkinson, B. A. *ACS Appl. Mater. Interfaces* **2014**, *6*, 9046−9052.
(20) Sliozberg, K.; Stein, H.; Khare, C.; Parkinson, B. A.; Ludwig, A.; Schuhmann, W. *ACS Appl. Mater. Interfaces* **2015**, *7*, 4883−4889.
(21) Mandlmeier, B.; Minar, N. K.; Feckl, J. M.; Fattakhova-Rohlfing, D.; Bein, T. *J. Mater. Chem. A* **2014**, *2*, 6504−6511.
(22) Kondofersky, I.; Dunn, H.; Müller, A.; Mandlmeier, B.; Feckl, J. M.; Fattakhova-Rohlfing, D.; Scheu, C.; Peter, L. M.; Bein, T. *ACS Appl. Mater. Interfaces* **2015**, *7*, 4623−4630.
(23) Strecker, A.; Salzberger, U.; Mayer, J. *Prakt. Metallogr.* **1993**, *30*, 482−495.
(24) Klahr, B. M.; Martinson, A. B. F.; Hamann, T. W. *Langmuir* **2011**, *27* (1), 461−468.
(25) Le Bail, A.; Duroy, H.; Fourquet, J. L. *Mater. Res. Bull.* **1988**, *23*, 447−452.
(26) Moulder, J.; Stickle, W.; Sobol, P.; Bomben, K. *Handbook of X-ray Photoelectron Spectroscopy*; Perkin-Elmer Corporation: Eden Prairie, MN, 1992.
(27) Biesinger, M. C.; Payne, B. P.; Grosvenor, A. P.; Lau, L. W. M.; Gerson, A. R.; Smart, R. S. C. *Appl. Surf. Sci.* **2011**, *257*, 2717−2730.
(28) Galtayries, A.; Warocquier-Clérout, R.; Nagel, M. D.; Marcus, P. *Surf. Interface Anal.* **2006**, *38*, 186−190.
(29) Wiberg, E.; Wiberg, N. *Inorganic Chemistry*; Academic Press: 2001.
(30) Strohmeier, B. R. *Surf. Interface Anal.* **1990**, *15*, 51−56.
(31) Steinwehr, H.E.v. *Z. Kristallogr. Miner.* **1967**, *125*, 377−403.
(32) Małecki, A.; Małecka, B.; Gajerski, R.; Łabuś, S. S. *J. Therm. Anal. Calorim.* **2003**, *72*, 135−144.
(33) Wieczorek-Ciurowa, K.; Kozak, A. J. *J. Therm. Anal. Calorim.* **1999**, *58* (3), 647−651.
(34) El-Shereafy, E.; Abousekkina, M. M.; Mashaly, A.; El-Ashry, M. *J. Radioanal. Nucl. Chem.* **1998**, *237*, 183−186.
(35) Fu, Y.; Chen, J.; Zhang, H. *Chem. Phys. Lett.* **2001**, *350*, 491−494.
(36) Tilley, S. D.; Cornuz, M.; Sivula, K.; Grätzel, M. *Angew. Chem., Int. Ed.* **2010**, *49*, 6405−6408.
(37) Cesar, I.; Sivula, K.; Kay, A.; Zboril, R.; Grätzel, M. *J. Phys. Chem. C* **2009**, *113*, 772−782.
(38) Fattakhova-Rohlfing, D.; Zaleska, A.; Bein, T. *Chem. Rev.* **2014**, *114*, 9487−9558.
(39) Woodcock, L. V. *Nature* **1997**, *385*, 141−143.
(40) Schroden, R. C.; Al-Daous, M.; Blanford, C. F.; Stein, A. *Chem. Mater.* **2002**, *14*, 3305−3315.
(41) Waterhouse, G. I. N.; Waterland, M. R. *Polyhedron* **2007**, *26*, 356−368.
(42) Peter, L. M.; Wijayantha, K. U.; Tahir, A. A. *Faraday Discuss.* **2012**, *155*, 309−322.




DOI: 10.1021/jacs.5b08040
*J. Am. Chem. Soc.* 2016, 138, 1860−1867

(43) Dunn, H. K.; Feckl, J. M.; Muller, A.; Fattakhova-Rohlfing, D.; Morehead, S. G.; Roos, J.; Peter, L. M.; Scheu, C.; Bein, T. *Phys. Chem. Chem. Phys.* **2014**, *16*, 24610−24620.
(44) Peter, L.; Ponomarev, E.; Fermin, D. *J. Electroanal. Chem.* **1997**, *427*, 79−96.
(45) Ponomarev, E.; Peter, L. *J. Electroanal. Chem.* **1995**, *396*, 219−226.
(46) Praveen, C. S.; Timon, V.; Valant, M. *Comput. Mater. Sci.* **2012**, *55*, 192−198.
(47) Shen, S.; Jiang, J.; Guo, P.; Kronawitter, C. X.; Mao, S. S.; Guo, L. *Nano Energy* **2012**, *1*, 732−741.
(48) Kleiman-Shwarsctein, A.; Hu, Y.-S.; Forman, A. J.; Stucky, G. D.; McFarland, E. W. *J. Phys. Chem. C* **2008**, *112*, 15900−15907.
(49) Kleiman-Shwarsctein, A.; Huda, M. N.; Walsh, A.; Yan, Y.; Stucky, G. D.; Hu, Y.-S.; Al-Jassim, M. M.; McFarland, E. W. *Chem. Mater.* **2010**, *22*, 510−517.
(50) Maeda, K.; Domen, K. *J. Phys. Chem. Lett.* **2010**, *1*, 2655−2661.
(51) Maeda, K.; Teramura, K.; Lu, D.; Saito, N.; Inoue, Y.; Domen, K. *Angew. Chem., Int. Ed.* **2006**, *45* (46), 7806−7809.



DOI: 10.1021/jacs.5b08040
*J. Am. Chem. Soc.* 2016, 138, 1860−1867